Structural and Multidisciplinary Optimization (2022) 65:160
https://doi.org/10.1007/s00158-022-03252-7

RESEARCH PAPER

Geometric dimensionality control of structural components in topology optimization

Nikolai Gerzen[1] · Thorsten Mertins[2] · Claus B. W. Pedersen[3]

Received: 21 December 2021 / Revised: 8 March 2022 / Accepted: 13 April 2022 / Published online: 14 May 2022

Abstract
The present contribution derives a theoretical framework for constructing novel geometrical constraints in the context of density-based topology optimization. Principally, the predefined geometrical dimensionality is enforced locally on the components of the optimized structures. These constraints are defined using the principal values (singular values) from a singular value decomposition of points clouds represented by elemental centroids and the corresponding relative density design variables. The proposed approach is numerically implemented for demonstrating the designing of lattice or membrane-like structures. Several numerical examples confirm the validity of the derived theoretical framework for geometric dimensionality control.

Keywords Manufacturing constraints · Topology optimization · Geometric constraints · Gradient based structural optimization · Lattice designing · Additive manufacturing

1 Introduction

Highest possible design freedom is one of the main advantages using nonparametric structural optimizations. However, enforcing geometric features of optimized designs is often a crucial point due to the lack of control over the geometric features. To address this problem a new type of constraints is suggested for sensitivity based optimization disciplines as topology, shape, sizing and bead optimizations. These constraints are visually interpretable and their usage is intuitive. Only geometric information is applied for evaluating them. Theoretically, the proposed approach is not limited to specific structural nonparametric optimization disciplines, but is also valid, for example, for multiphysics optimization such as CFD, thermo-mechanical, electro-mechanical and fluid-structural, where the values from a singular value decomposition (SVD) of the design variables clouds can be determined and used to define additional constraints to enforce geometric features. However, the present work demonstrates the capabilities of the suggested approach in the context of gradient based structural topology optimization of lattice-like structures.

Local dimensionality is explained in the following using a small illustrative example. Figure 1a introduces a very coarse finite element model of a simple cube clamped at the bottom corners and applied to a top load. The classic topology optimization minimizing the compliance subjected to a volume constraint yields the design shown in Fig. 1b. Geometric properties of the optimized structure can be locally investigated considering vicinities (blue spheres shown at Fig. 1) with some predefined radius at certain locations depending on the design requirements. Relatively to the present radius the considered structural components are rather bulky and thick compared to the 3D space as shown in Fig. 1b.

Adding constraints for the SVD values to the optimization problem enforce 1D lattice-like and 2D membrane-like structures locally for the optimized results as shown in Fig. 2a and b, respectively. Again, the dimensionality assessment is relative with respect to the predefined radius of the

Responsible Editor: Emilio Carlos Nelli Silva

✉ Nikolai Gerzen
nikolai.gerzen@th-owl.de

1 Department of Civil Engineering, OWL University of Applied Sciences and Arts, Emilienstraße 45, 32756 Detmold, Germany

2 Dassault Systemes Deutschland GmbH, Albert-Nestler-Str. 17, 76131 Karlsruhe, Germany

3 Dassault Systemes Deutschland GmbH, Glockengiesserwall 22, 20095 Hamburg, Germany

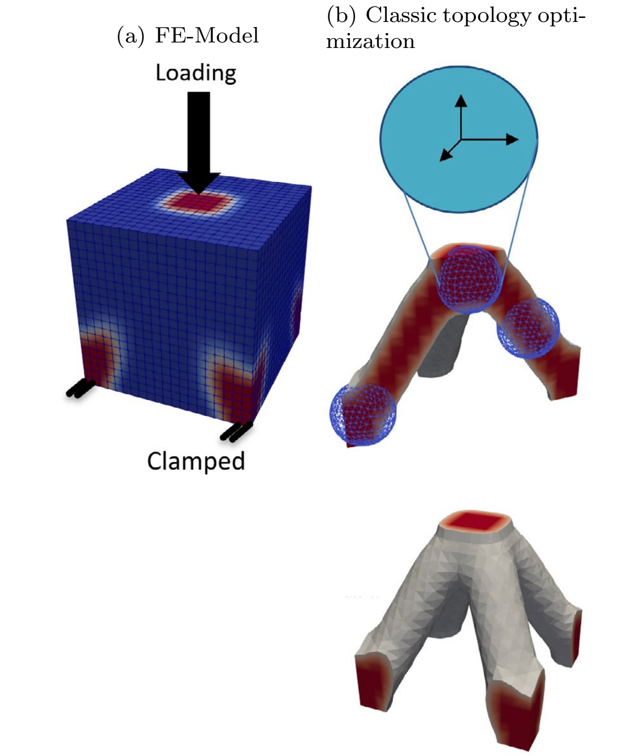

Fig. 1 Topology optimization minimizing compliance subject to a volume constraint. The content of this figure is: (a) FE-model and (b) classic topology optimization. No additional constraints for geometric dimensionality are applied. The structural components are rather bulky and thick within a given radius of a search vicinity [blue sphere in (**b**)]. (Color figure online)

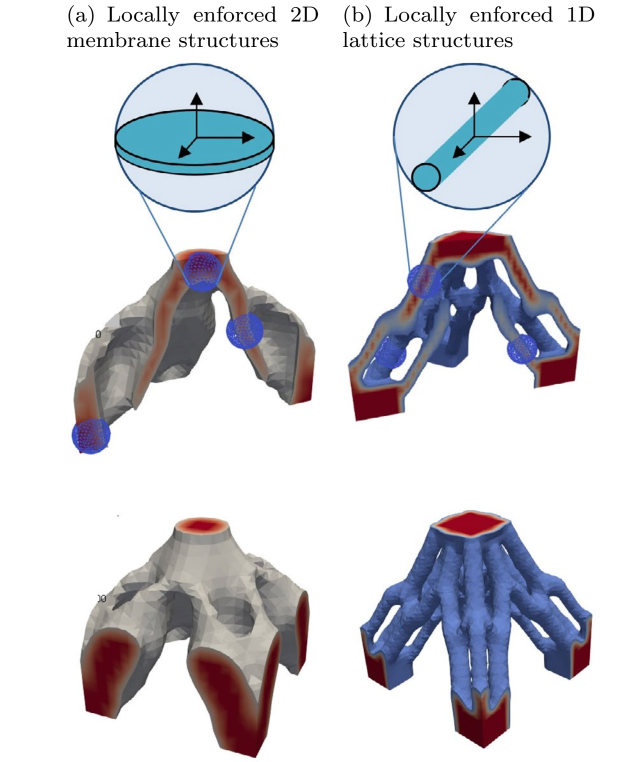

Fig. 2 Topology optimization minimizing compliance subject to a volume constraint and constraints locally enforcing the dimensionality for the structural components. The content of this figure is: (a) locally enforced 2D membrane structures and (b) locally enforced 1D lattice structures

considered vicinity. Note, the focus of the present work is on lattice-like structures. Strictly membrane-like structures will be addressed in future work.

Possible fields of application are shortly summarized in the following. The present method can be employed for a variety of real-world design applications. Avoiding bulky areas of the component with high material concentrations for indirectly controlling cooling or flow of the metallic porosity for casting produced components by enforcing 1D or 2D layouts. The orientations of structural components, for example, for ribs and lattice designing, can be enforced to ensure the feasibility of a molding process. Ensure the removeability of powder for a 3D printed design enforcing 1D layouts. Ensure continuous fiber printing having no crossing fibers by enforcing 1D layout.

Competitive approaches exist for nonparametric optimization methods (topology, shape, bead and sizing) enforcing geometric properties on the designs directly or indirectly to fulfill various manufacturing process requirements and/or geometric design principles and/or required visual effects. In the following these approaches will be outlined. Note, many other approaches exist being comparable to the outlined publications or a subset of these. However, none of these existing approaches for enforcing geometric properties on the designs for nonparametric optimization are based upon constraining the values from a singular value decomposition (SVD) of the design variables.

Filter techniques and projection methods are also called regularization techniques. One of the most common is the density variable filter for topology optimization where the relative densities are the design variables being filtered, for example, Bendsøe and Sigmund (2004), Luo et al. (2019), Sigmund and Petersen (1998), Lazarov et al. (2016), Zhou et al. (2015), Lazarov and Wang (2017) and references therein. The filter techniques and the projection methods can be combined for enforcing a length scale and thereby, ensuring a manufacturable structure for member size requirements, for example, for casted manufactured structures, 3D printed structures, milled structures, etc. Our present approach can also enforce member sizes through a radius but the present approach is fundamentally different.

Direct parametrization of design variables is addressed, for example, in Zhang et al. (2018), Leiva et al. (2004), Gersborg and Andreasen (2011) for obtaining feasible designs for casted structures and plate manufactured structures. Our present method does not include any parametrization or mapping of the design variables, but it could be applied for obtaining feasible designs for plate manufactured structures. This will be addressed in future work.

Penalty functions and projection functions The authors in Langelaar (2017, 2019), Hoffarth et al. (2017) apply penalty functions to ensure geometric feasible designs for additive manufacturing (3D printing) and multiaxis machining. The work in Vatanabe et al. (2016) and Carstensen and Guest (2018) illustrates the ability of the projection schemes to efficiently apply geometric control for the optimization solutions so the designs are geometrically feasible for manufacturing. The authors in Norato (2018) and Zhang et al. (2016), employ the geometry projection method to project an analytical description of a set of geometric primitives and fixed-thickness plates, respectively. This enforces the structural members to be super shapes or plates for manufacturability. Our present approach could also enforce plate-like structures but is fundamentally different from penalty functions or projection functions.

Local volume constraints The authors in Wu et al. (2017, 2018), Schmidt et al. (2019), Liu et al. (2021) apply local volume constraint approaches enforcing geometrically porous like structures. Such constraint can also be applied to mimic lattice-like structures in 2D and membrane-like structures in 3D. Our present approach can also enforce lattice-like and membrane-like structures but is fundamentally different than the local volume constraint approaches.

Heuristic methods The work in Strömberg (2010) applies a heuristic method updating the move limits in each optimization iteration defined such that the draw constraints are satisfied. Thereby, no explicit constraint appears in the nested formulation except for the lower and upper limits on the design variables, but these move limits updates are fully heuristic. The work in Dienemann et al. (2017) applies a midsurface approach by calculating the average of the element coordinates in the punch direction for achieving deep drawing manufactured structures. The implementation of this approach is more heuristic, as the movement of the mid surface at a constant wall thickness is not consistently included in the mathematical sensitivity calculation. This is seen by the increased number of optimization iterations. Both the methods in Strömberg (2010) and Dienemann et al. (2017) are partially mathematically inconsistent being heuristic whereas our present approach is mathematically consistent and could also enforce structures suitable for deep drawing, but the approach is fundamentally different to the heuristic methods.

Scope of the paper The structure of the present paper is as follows. In Sect. 2 the utilized structural optimization framework is briefly outlined. The calculation and the interpretation of local geometric properties using SVD are explained in Sect. 3. Especially, the advantages and limitations of the suggested approach are discussed. Section 4 introduces SVD based constraints which can be used to control the geometric dimensionality of optimized structural components. The potential of the proposed approach is demonstrated in Sect. 5 on a number of 2D and 3D examples. The obtained numerical findings and potential next steps are summarized in Sect. 6.

2 Topology optimization implementation and workflow

The aim of the present work is to examine the impact of constraints based on SVD of design variables clouds for the geometric features of optimized structures. Evaluating of these constraints requires processing of pure geometric information. Within this section, the utilized optimization workflow is only outlined. Practically, the suggested geometric control is implemented in the optimization software SIMULIA Tosca Structure Dassault Systèmes (2021b) using mathematical programming for updating the design variables and the adjoint sensitivities implemented in SIMULIA Abaqus Dassault Systèmes (2021a) for the structural finite element models. The direct solver in SIMULIA Abaqus is applied for solving the equilibrium $\boldsymbol{R} = \mathbf{0}$ of the finite element model and the adjoint solution except for the numerical results shown in Sects. 5.2 and 5.3 where the iterative algebraic multi-grid solver by SIMULIA Abaqus is applied. Note, that both the direct finite element solver and the iterative algebraic multi-grid solver can solve nonlinear structural modeling such as contacts, large deformations and constitutive nonlinear material models. However, here we show linear structural applications. Furthermore, all the present numerical topology optimization results are generated using the so-called SIMP-model Bendsøe and Sigmund (2004) for the constitutive material being proportional to a powerlaw of the relative elemental density $0.001 \leq \rho_e \leq 1.0$. Thereby, the Young's modulus E_e in a finite element e is interpolated using $E_e = E\rho_e^p$ and where $p = 3$ is kept constant during the optimization iterations. The design variables vector $\boldsymbol{\rho}$ contains the relative densities of all structural elements in the design domain.

The numerical optimization results shown in Sects. 5.1 and 5.2 have the following optimization framework of minimizing the compliance C (maximizing the stiffness) for the given external loading $\boldsymbol{P}$ and the resulting displacements $\boldsymbol{U}$:

$$
\begin{aligned}
&\text{Minimize compliance:}\\
&\qquad C(\boldsymbol{U}(\boldsymbol{\rho})) = \boldsymbol{P}^T \boldsymbol{U}(\boldsymbol{\rho}) \quad \underset{\boldsymbol{\rho}\in\mathbb{R}^n}{\longrightarrow} \quad \min\\
&\text{s.t.}\\
&\text{structural equilibrium constraint:}\\
&\qquad \boldsymbol{R}(\boldsymbol{\rho}, \boldsymbol{U}(\boldsymbol{\rho})) = \boldsymbol{K}(\boldsymbol{\rho})\boldsymbol{U}(\boldsymbol{\rho}) - \boldsymbol{P} = \boldsymbol{0},\\
&\text{relative mass constraint:}\\
&\qquad m(\boldsymbol{\rho}) \le f m_{\text{full}},\\
&\text{box constraints:}\\
&\qquad 0.001 \le \rho_e \le 1.0,\\
&\text{constraints on singular values:}\\
&\qquad \bar{s}_{min}(\boldsymbol{\rho}) \le \bar{s}^*_{min} \quad \text{and/or}\\
&\qquad \bar{s}_{mid}(\boldsymbol{\rho}) \le \bar{s}^*_{mid}.
\end{aligned}
\tag{1}
$$

The total mass $m(\boldsymbol{\rho})$ of the design domain is constrained to fulfill a certain weight target defined by the relative material fraction f and m_{full} being the mass of the design domain having full material. A sensitivity filter is applied for regularization introducing a length scale and for suppressing checkerboards, see Sigmund and Maute (2013), Sigmund and Petersen (1998). The radius of the sensitivity filter R_f for all present optimization results is 1.3 of the averaged element size of all elements specified in the design domain.

The examples shown in Sect. 5.3 have the mass as the design response to be minimized as objective function for a strength optimization. The constrained design response is the Von-Mises stress $\boldsymbol{s}_v(\boldsymbol{\rho}, \boldsymbol{U}(\boldsymbol{\rho}))$ of the elemental integration points being applied as a single aggregated constraint $A(\boldsymbol{s}_v(\boldsymbol{\rho}, \boldsymbol{U}(\boldsymbol{\rho})))$ as follows:

$$
\begin{aligned}
&\text{Minimize mass: } m(\boldsymbol{\rho})\\
&\text{s.t.}\\
&\text{structural equilibrium constraint:}\\
&\qquad \boldsymbol{R}(\boldsymbol{\rho}, \boldsymbol{U}(\boldsymbol{\rho})) = \boldsymbol{K}(\boldsymbol{\rho})\boldsymbol{U}(\boldsymbol{\rho}) - \boldsymbol{P} = \boldsymbol{0},\\
&\text{stress constraint:}\\
&\qquad A(\boldsymbol{s}_v(\boldsymbol{\rho}, \boldsymbol{U}(\boldsymbol{\rho}))) \le s_C,\\
&\text{box constraints:}\\
&\qquad 0.001 \le \rho_e \le 1.0,\\
&\text{constraints on singular values:}\\
&\qquad \bar{s}_{min}(\boldsymbol{\rho}) \le \bar{s}^*_{min} \quad \text{and/or}\\
&\qquad \bar{s}_{mid}(\boldsymbol{\rho}) \le \bar{s}^*_{mid}.
\end{aligned}
\tag{2}
$$

where s_C is the stress constraint value. The stress design response $\boldsymbol{s}_v(\boldsymbol{\rho}, \boldsymbol{U}(\boldsymbol{\rho}))$ in Eq. 2 is applied using a relaxation similar to Bruggi (2008), Holmberg et al. (2013). In addition, an aggregation function $A(\boldsymbol{s}_v(\boldsymbol{\rho}, \boldsymbol{U}(\boldsymbol{\rho})))$ in the form of a p-norm approach is applied for the elemental stresses at integration points similar to Bruggi (2008), Holmberg et al. (2013), Verbart et al. (2015), París et al. (2008) avoiding having many design responses as the stress at each integration point is applied in the constraint.

3 Calculation of local geometric properties of structural components using SVD

For the present approach, new measures are introduced as design responses for the topology optimization. These measures can either be applied in the objective function or as constraints to locally enforce certain geometric features of the

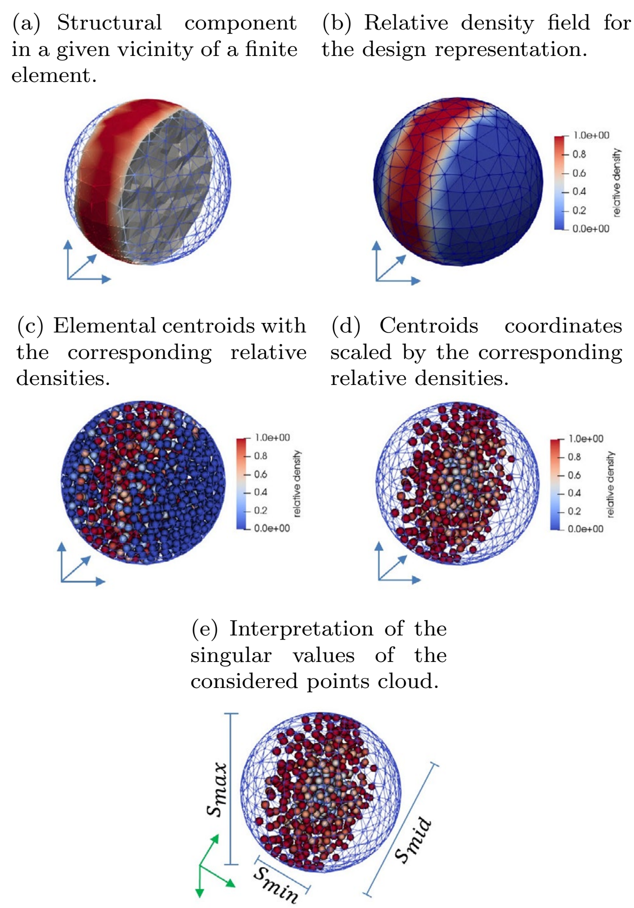

Fig. 3 Evaluation of the relative density field of a 3D finite element model by Singular Value Decomposition (SVD) within a sphere having a given radius. As a result the three singular values (s_{min}, s_{mid}, s_{max}) related to the three dimensions of the object and the corresponding orientations/vectors (shown in green) are determined. The content of this figure is: (a) structural component in a given vicinity of a finite element, (b) relative density field for the design representation, (c) elemental centroids with the corresponding relative densities, (d) centroids coordinates scaled by the corresponding relative densities and (e) interpretation of the singular values of the considered points cloud. (Color figure online)

optimized structures. Mathematically, the measures are based on singular values (or the corresponding vectors) of a matrix describing the design variables distribution within a given vicinity (for example, a sphere having a given radius). In the context of topology optimization then the distribution of the design variables (relative densities) around each finite element (a sphere with a given radius, see Fig. 3a) is evaluated using Singular Value Decomposition (SVD). The obtained singular values (s_{max}, s_{mid} and s_{min}, see Fig. 3e) are related to three geometrical dimensions of the geometric object described by the density field of the considered sphere. These measured values are used to construct the design responses for the structural optimization enforcing local geometric control.

3.1 Singular values of a relative density field

In the following we assume that for a given finite element mesh with n finite elements that the corresponding centroid coordinates $\boldsymbol{C} \in \mathbb{R}^{n\times 3}$ are defined as

$$\boldsymbol{C} = \begin{bmatrix} x_1 & y_1 & z_1 \\ \vdots & \vdots & \vdots \\ x_n & y_n & z_n \end{bmatrix} \tag{3}$$

and the relative densities $\boldsymbol{\rho} \in \mathbb{R}^n$ where $0.0 < \rho_i \leq 1.0$ are given for each optimization iteration. For the evaluation of the geometric properties of the structural components (Fig. 3a), represented by the relative density field (Fig. 3b), in a given vicinity with the radius R around a finite element $e \in \{1, ..., n\}$ then the m neighboring elements $j \in \{1, ..., m\}$ and their centroids $\breve{\boldsymbol{C}} \in \mathbb{R}^{m\times 3}$ (Fig. 3c), are determined by the following condition

$$\left\| \boldsymbol{C}_e - \boldsymbol{C}_j \right\| \leq R. \tag{4}$$

The quantities $\boldsymbol{C}_e$ and $\boldsymbol{C}_j$ corresponds to the e-th and j-th lines of $\boldsymbol{C}$. The corresponding relative densities are represented by $\breve{\boldsymbol{\rho}} \in \mathbb{R}^m$. The data stored in $\breve{\boldsymbol{C}}$ must be centered around its mean before applying SVD as

$$\hat{\boldsymbol{C}}_j = \breve{\boldsymbol{C}}_j - \frac{1}{\sum_{i=1}^m \breve{\rho}_i} \left[\sum_{i=1}^m \breve{x}_i \breve{\rho}_i \quad \sum_{i=1}^m \breve{y}_i \breve{\rho}_i \quad \sum_{i=1}^m \breve{z}_i \breve{\rho}_i \right]. \tag{5}$$

Equation (5) corresponds to a shift of the global coordinate system to the center of gravity for the considered points of a given cloud. The relative density values are now used to scale the shifted centroid coordinates stored in $\hat{\boldsymbol{C}}$ as following

$$\tilde{\boldsymbol{C}} = \begin{bmatrix} \hat{x}_1 \breve{\rho}_1 & \hat{y}_1 \breve{\rho}_1 & \hat{z}_1 \breve{\rho}_1 \\ \vdots & \vdots & \vdots \\ \hat{x}_m \breve{\rho}_m & \hat{y}_m \breve{\rho}_m & \hat{z}_m \breve{\rho}_m \end{bmatrix}. \tag{6}$$

Centroid coordinates of elements representing solid material ($\breve{\rho}_j = 1.0$) are not changed by this operation. However, elements representing intermediate material or partial void ($\breve{\rho}_j < 1.0$) have their corresponding centroids moved in the direction of the center of gravity for the considered points in the cloud (Fig. 3d). The singular values $0 \leq s_{min} \leq s_{mid} \leq s_{max}$ for each vicinity are obtained through the SVD of the matrix $\tilde{\boldsymbol{C}}$ as

$$\begin{gathered} \tilde{\boldsymbol{C}} = \boldsymbol{W} \begin{bmatrix} s_{max} & 0 & 0 \\ 0 & s_{mid} & 0 \\ 0 & 0 & s_{min} \end{bmatrix} \boldsymbol{V}^T, \\ \boldsymbol{W} \in \mathbb{R}^{m\times m}, \quad \boldsymbol{V} = \left[\boldsymbol{v}_{max}\ \boldsymbol{v}_{mid}\ \boldsymbol{v}_{min} \right], \\ \boldsymbol{v}_k \in \mathbb{R}^3 \quad \text{and} \quad k \in \{min,\ mid,\ max\}. \end{gathered} \tag{7}$$

These quantities represent the major local dimensions of the object described by the considered relative density field, see Fig. 3e. The corresponding right singular vectors $\boldsymbol{v}_k$ (shown in green) represent the directions of the major dimensions and are orthogonal to each other. The orthonormal square matrix $\boldsymbol{W} \in \mathbb{R}^{m\times m}$ contains the left singular vectors which are neither applied nor interpreted in the present work. Note, the Matrix $\boldsymbol{W}$ is part of the considered decomposition and is introduced for completeness. It is not necessary to calculate and to store this matrix as explained in Sect. 3.2. Afterwords we need to normalize the singular values s_k by the largest singular value $\hat{s}_{max}$ of matrix $\hat{\boldsymbol{C}}$ as the following

$$\bar{s}_k = \frac{s_k}{\hat{s}_{max}}. \tag{8}$$

Thereby, the singular values are invariant with respect to the absolute size of the considered vicinity. Note, matrix $\hat{\boldsymbol{C}}$ corresponds to matrix $\tilde{\boldsymbol{C}}$ in which all the relative densities are set to $\breve{\rho}_j = 1.0$ representing the largest possible instance for the local structural component of a given design.

3.2 Relation between singular values and eigenvalues

Numerous algorithms for the eigenvalue decomposition can be reused to perform the SVD calculation of the matrix $\tilde{\boldsymbol{C}} \in \mathbb{R}^{m\times 3}$ and especially, if they are already available in the applied finite element software environment. Therefore, we introduce the square matrix as

$$\boldsymbol{Q} = \tilde{\boldsymbol{C}}^T \tilde{\boldsymbol{C}} \quad \text{with} \quad \boldsymbol{Q} \in \mathbb{R}^{3\times 3}. \tag{9}$$

Then the decomposition of the matrix in Eq. (9)

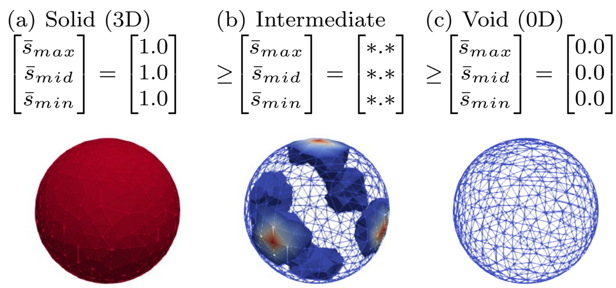

Fig. 4 Normalized singular values of relative density fields for solid (3D object representation) versus void (0D object representation) structural elements. The content of this figure is: (a) solid (3D), (b) intermediate and (c) void

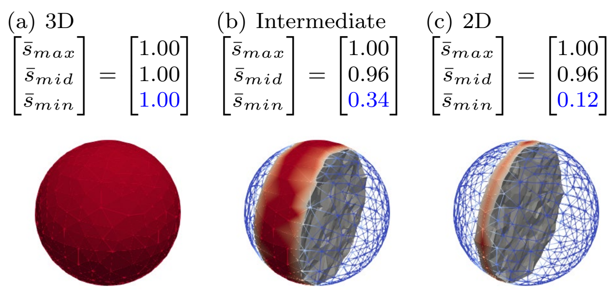

Fig. 5 Normalized singular values of relative density fields for solid (3D object representation) transforming to a shell, plate or membrane material layout (2D object representation). The content of this figure is: (a) 3D, (b) Intermediate and (c) 2D

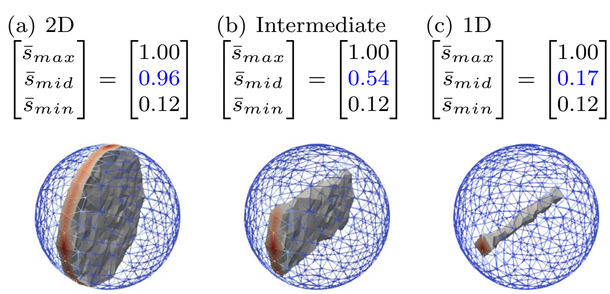

Fig. 6 Normalized singular values of relative density fields for shell, plate or membrane layout (2D object representation) transforming to a beam, bar or lattice material layout (1D object representation). The content of this figure is: (a) 2D, (b) Intermediate and (c) 1D

$$\boldsymbol{Q}=\boldsymbol{V}\begin{bmatrix}\lambda_{max} & 0 & 0\\ 0 & \lambda_{mid} & 0\\ 0 & 0 & \lambda_{min}\end{bmatrix}\boldsymbol{V}^T, \tag{10}$$

directly provides the singular vectors $\boldsymbol{v}_k$ and the corresponding singular values are obtained from the eigenvalues of the matrix $\boldsymbol{Q}$ as follows

$$s_k=\sqrt{\lambda_k}. \tag{11}$$

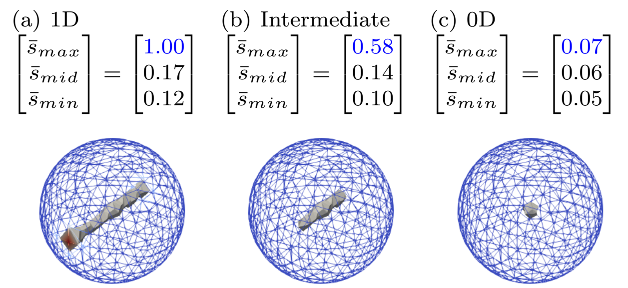

Fig. 7 Normalized singular values of relative density fields for beam, bar or lattice layout (1D object representation) transforming to a point or void material layout (0D object representation). The content of this figure is: (a) 1D, (b) intermediate and (c) 0D

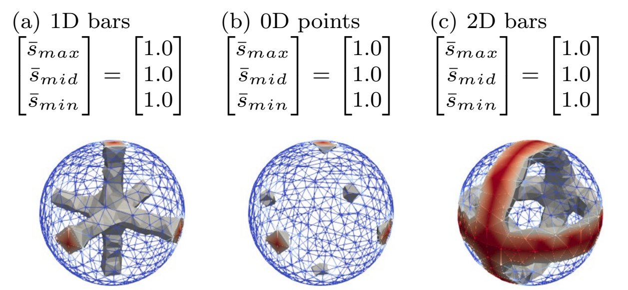

Fig. 8 Normalized singular values all being 1.00 of relative density fields representing assemblies of 2D, 1D or 0D parts in a 3D space. The content of this figure is: (a) 1D bars, (b) 0D points and (c) 2D bars

Note, there is no need to calculate and to store the matrix $\boldsymbol{W}$ introduced in Eq. (7).

3.3 Geometric interpretations of the singular values

Figures 4, 5, 6, 7 and 8 shows the normalized values $\bar{s}_k$ for different exemplary structural layouts of the design variables (relative densities) in a finite elements setting for topology optimization. All the normalized singular values are equal to 1.0 for a fully solid sphere and are equal to 0.0 for a void sphere as shown in Fig. 4. The singular values are between 0.0 and 1.0 for all other material layout configurations.

One of the singular values approaches zero when a fully solid 3D object transforms to a 2D object as shown in Fig. 5. In this case 2D means a shell, plate or membrane-like material layout.

Two singular values approach zero when a 2D object is transforming to a 1D object as shown in Fig. 6. Beam, bar or lattice-like material layouts corresponds to 1D objects.

All singular values approach zero when a 1D object transforms to an empty sphere (void) as shown in Fig. 7.

Consequently, the singular values as illustrated in Figs. 4, 5, 6 and 7 can be used to formulate new types of constraints for controlling and enforcing geometric features of the optimized structures. Such constraints will be introduced in the following sections.

3.4 Limitations of the approach

Note, that the dimensionality of the geometric object calculated using singular values describes how much space the object has within a considered vicinity (sphere). Therefore, the size of the sphere must be properly chosen depending on the specific applications. Rather small spheres should be applied for locally controlling the structural dimensionality. Frequently, for practical applications using larger spheres can lead to misinterpretation of the structural dimensionality for the optimization algorithm. For example, an assembly of 1D or 0D parts can be interpreted as a fully solid 3D object as shown in Fig. 8. However, as the numerical examples for the present work mainly apply spheres having relative small radius then this has not been observed as a critical issue for the present applications.

4 Locally constraining the dimensionality of structural components

Singular values derived in the previous sections are now used to construct new types of design responses for topology optimization. Constraints for local control of structural dimensionality are formulated using these design responses.

4.1 Eliminating discontinuities for singular values

Similar to eigenfrequency optimizations, see for example Seyranian et al. (1994) and Seyranian (1987), where in case of multiple eigenvalues the corresponding modes, i.e. eigenvectors, can switch their order between the optimization iterations, the order of singular vectors can switch in case of multiple singular values. In both cases this behavior leads to discontinuities of design responses based on eigenvalues or on singular values, as the corresponding derivatives are directly depending on eigenvectors or on singular vectors, see for example Eq. (23). Therefore, singular values based design responses for a gradient based optimization algorithm require a smooth transition between the singular values. This is obtained using smooth approximations, see for example Kennedy and Hicken (2015), for the maximum and minimum singular values as

$$
\begin{aligned}
s_{smax} &= \frac{\sum_{k=1}^{3} s_k e^{p(s_k - r)}}{\sum_{k=1}^{3} e^{p(s_k - r)}} \quad \text{where} \quad p = 6, \\
s_{smin} &= \frac{\sum_{k=1}^{3} s_k e^{p(s_k - r)}}{\sum_{k=1}^{3} e^{p(s_k - r)}} \quad \text{where} \quad p = -6,
\end{aligned}
\tag{12}
$$

and

$$
s_{smid} = \left(\sum_{k=1}^{3} s_k \right) - s_{smax} - s_{smin}.
$$

The quantity r is used here to overcome numerical issues for high exponent values and is usually set to $r = s_{max}$ or to $r = s_{min}$ approximating the maximum or the minimum values, respectively.

4.2 Design responses based upon singular values

For a given vicinity of a finite element $i \in \{1, ..., n\}$, we consider the three following measures

$$
\begin{aligned}
\bar{s}^i_{min} &= \frac{s^i_{smin}}{\hat{s}^i_{max}}, \\
\bar{s}^i_{mid} &= \frac{s^i_{smid}}{\hat{s}^i_{max}}, \\
\bar{s}^i_{mid2max} &= \frac{s^i_{smid}}{s^i_{smax}}.
\end{aligned}
\tag{13}
$$

The quantities $\bar{s}^i_{min}$ and $\bar{s}^i_{mid}$ describe locally the smallest and the second smallest dimensions of the structural element. These quantities are normalized by the maximum possible dimension of the considered vicinity and thereby, invariant with respect to the absolute vicinity size. The third quantity $\bar{s}^i_{mid2max}$ is a relation between the second largest dimension and the largest dimension. Note, that $\bar{s}^i_{mid2max}$ is per definition a relative quantity and does not directly contain $\hat{s}^i_{max}$. Assume that the design domain consists of all finite elements then the quantities $\bar{s}^i_{min}$ and $\bar{s}^i_{mid}$ are aggregated over all finite elements using smooth maximum approximations as these will be used to formulate less-equal constraints. The quantities $\bar{s}^i_{mid2max}$ are aggregated using smooth minimum approximation as these will be used to formulate greater-equal constraints. With $q \in \{min\ , mid\ , mid2max\}$ then the three following design responses are introduced

$$
\begin{aligned}
&\bar{s}_q = \frac{\sum_{i=1}^{n} \bar{s}^i_q e^{p\bar{s}^i_q}}{\sum_{i=1}^{n} e^{p\bar{s}^i_q}} \\
&\text{where for the following equations:} \\
&n = \text{total number of elements}, \\
&p = 6 \quad \text{for} \quad q = min \quad \text{or} \quad q = mid, \\
&\text{and} \quad p = -6 \quad \text{for} \quad q = min2max.
\end{aligned}
\tag{14}
$$

Note, smooth maximum and minimum approximations are used here to obtain just three scalar design responses for the whole design domain. These design responses are applied in the following sections to formulate constraints for the optimization. Smooth approximations are more general compared to the so-called p-norms, for example, negative and positive values can be approximated.

4.3 Constraints for gradient based optimization

To locally control the dimensionality of structural elements the following constraints are constructed.

Locally enforce 1D or 2D structural elements by constraining the smallest dimension. Thereby, 3D fully solid material objects are eliminated within a given vicinity. This is obtained by applying the following constraint

$$\bar{s}_{min} \leq \bar{s}^*_{min} \tag{15}$$

where $0.0 < \bar{s}^*_{min} < 1.0$. This constraint causes the designs to be membrane or lattice-like structures as the constraint avoids bulky material concentrations. Thereby, the value $\bar{s}^*_{min}$ implicitly prescribes the maximal thickness of a lattice or a membrane member relatively to the diameter of the considered vicinity.

Locally enforce 1D structural elements by simultaneously constraining the smallest and the second smallest dimensions. Thereby, 2D and 3D objects are eliminated within a given vicinity. Hence, we apply the following constraints

$$\bar{s}_{min} \leq \bar{s}^*_{min} \quad \text{and} \quad \bar{s}_{mid} \leq \bar{s}^*_{mid} \tag{16}$$

where $0.0 < \bar{s}^*_{min} < 1.0$ and $\bar{s}^*_{min} < \bar{s}^*_{mid} < 1.0$. These constraints cause the designs to be lattice-like structures and avoid bulky material concentrations and membrane-like structures. The value $\bar{s}^*_{mid}$ implicitly prescribes the maximal width of lattice members relatively to the diameter of the considered vicinity and controls the curvature. If this value is chosen too small the optimizer will not be able to generate joints between 1D components. Sometimes such behavior is intended, for example, for avoiding fiber crossing in a composite optimization. Increasing the value $\bar{s}^*_{mid}$ allow the curvature of the structural components to be increased.

Locally enforce 2D structural elements by constraining the smallest dimension and the relation between the second largest and the largest dimensions. Thereby, 1D and 3D objects are eliminated. This is obtained by applying the following constraints

$$\bar{s}_{min} \leq \bar{s}^*_{min} \quad \text{and} \quad \bar{s}_{mid2max} \geq \bar{s}^*_{mid2max} \tag{17}$$

where $0.0 \leq \bar{s}^*_{min} \leq 1.0$ and $0.5 \leq \bar{s}^*_{mid2max} \leq 1.0$. These constraints cause the designs to be membrane-like structures and to avoid bulky material concentrations and lattice-like structures. Again the value $\bar{s}^*_{min}$ implicitly prescribes the maximal thickness of the membrane components and the value $\bar{s}^*_{mid2max}$ controls the dimensional proportions normal to the thickness direction. The value $\bar{s}^*_{min}$ also implicitly controls the curvature of membrane components. Smaller values lead to plane and large values for curved structures.

4.4 Relations between relative material fraction and geometric parameters

Figures 3, 4, 5, 6, 7 and 8 illustrates that the relative material fraction f_s of the sphere having the radius R is partially related to the geometric control imposed by constraining the singular values of the decomposition (SVD) for the design variables inside the sphere. The following guidelines for lattice are applied in the present numerical applications in 3D:

Lattice design—Figs. 6 and 7 shows certain typical lattice structures obtained constraining the singular values $\bar{s}_{min}$ and $\bar{s}_{mid}$ to be less than sudden values. Assuming that $\bar{s} = \bar{s}_{min} = \bar{s}_{mid}$ and that the volume $V_{lattice}$ of the lattice member is much smaller than the volume of sphere $V_{sphere} = \frac{4}{3}\pi R^3$ then the volume of the lattice is given by $V_{lattice} = \pi(R\bar{s})^2 2R$. Thereby, the relative material fraction in the sphere is $f_s = V_{lattice}/V_{sphere} = \frac{3}{2}\bar{s}^2$.

Minimum and maximum length scales - As specified in Sect. 2 a sensitivity filter is used for ensuring the optimization formulations in Eqs. (1) and (2) to be well-posed. Usually, a filter is introduced for avoiding the so-called checkerboards and secondly, to introduce a length scale Sigmund and Maute (2013), Sigmund and Petersen (1998). In the present approach $\bar{s}^*_{min}$ and the radius R introduces a maximum length scale

$$l_{max} = \bar{s}^*_{min} 2R \tag{18}$$

for one of the directions. Therefore, the optimization setup is ill-posed when the filter radius R_f is larger than $l_{max}/2$. Hence, the length scale for one of the directions has a lower bound being the doubled filter radius

$$l_{min} = 2R_f \qquad \text{using} \qquad l_{min} \overset{!}{<} l_{max} \tag{19}$$

and an upper bound to be l_{max}. Note, that other methods introducing a minimum length scale would also be feasible as long as the introduced length scale is lower than l_{max}.

4.5 Sensitivity analysis of SVD design responses

The derivatives of the design responses $\bar{s}_q$ introduced in Eq. (14) with respect to the relative densities ρ_e must be determined for gradient based optimization. The derivation of the corresponding sensitivity relations is based upon multiple applications of the chain rule to calculate the derivatives $\frac{\partial \bar{s}_q}{\partial \rho_e}$ as pure geometric quantities. In this section, the required partial derivatives are derived.

Derivatives of aggregated design responses with respect to dimensionality measures defined in Eqs. (13) and (14) yield

$$\frac{\partial \bar{s}_q}{\partial \bar{s}_q^i} = \frac{(1 + (\bar{s}_q^i - \bar{s}_q)p)e^{p\bar{s}_q^i}}{\sum_j^n e^{p\bar{s}_q^j}} \tag{20}$$

Derivatives of dimensionality measures with respect to smoothed singular values s_{smin}, s_{smid} and s_{smax} defined in Eq. (12) yield

$$\begin{aligned}
&\frac{\partial \bar{s}^i_{min}}{\partial s_{smin}} = \frac{1}{\hat{s}^i_{max}}, \quad \frac{\partial \bar{s}^i_{min}}{\partial s_{smid}} = 0, \quad \frac{\partial \bar{s}^i_{min}}{\partial s_{smax}} = 0,\\
&\frac{\partial \bar{s}^i_{mid}}{\partial s_{smin}} = 0, \quad \frac{\partial \bar{s}^i_{mid}}{\partial s_{smid}} = \frac{1}{\hat{s}^i_{max}}, \quad \frac{\partial \bar{s}^i_{mid}}{\partial s_{smax}} = 0\\
&\frac{\partial \bar{s}^i_{mid2max}}{\partial s_{smin}} = 0, \quad \frac{\partial \bar{s}^i_{mid2max}}{\partial s_{smid}} = \frac{1}{s^i_{smax}}\\
&\frac{\partial \bar{s}^i_{mid2max}}{\partial s_{smax}} = -\frac{s^i_{smid}}{(s^i_{smax})^2}.
\end{aligned} \tag{21}$$

Derivatives of smoothed singular values with respect to singular values s_{min}, s_{mid} and s_{max} defined in Eq. (11) yield

$$\begin{aligned}
&\frac{\partial s_{smin}}{\partial s_k} = (1 + p(s_k - s_{min}))e^{ps_k - r}\left(\sum_k e^{ps_k - r}\right)^{-1},\\
&\frac{\partial s_{smax}}{\partial s_k} = (1 + p(s_k - s_{max}))e^{ps_k - r}\left(\sum_k e^{ps_k - r}\right)^{-1},\\
&\frac{\partial s_{smid}}{\partial s_k} = \sum_k \left(\frac{\partial s_k}{\partial \rho}\right) - \frac{\partial s_{max}}{\partial \rho} - \frac{\partial s_{min}}{\partial \rho}
\end{aligned} \tag{22}$$

Derivatives of singular values with respect to relative densities $\breve{\rho}_j$ are obtained as following

$$\begin{aligned}
&\frac{\partial s_k}{\partial \breve{\rho}_j} = \frac{1}{2\sqrt{\lambda_k}}\frac{\partial \lambda_k}{\partial \breve{\rho}_j},\\
&\frac{\partial \lambda_k}{\partial \breve{\rho}_j} = \boldsymbol{v}_k^T \frac{\partial(\tilde{\boldsymbol{C}}^T \tilde{\boldsymbol{C}})}{\partial \breve{\rho}_j}\boldsymbol{v}_k.
\end{aligned} \tag{23}$$

Relations between the quantities ρ_e and $\breve{\rho}_j$ can be described by boolean operators. The corresponding derivatives are straight forward and are not outlined here.

4.6 Computational costs for SVDs

As explained in previous sections then the suggested constraints are based on SVDs of point clouds scaled by densities around each finite element in the model. The number of points is directly dependent on radius R for the considered vicinities similar to standard filter techniques known in the context of topology optimization. Therefore, this has no influence on the numerical costs for evaluating the constraint values as only the eigenvalue decomposition of matrix $\boldsymbol{Q} \in \mathbb{R}^{3\times3}$ is performed, see Sect. 3.2, in each optimization iteration for each finite element. However, performing the sensitivity analysis, Eq. (23) must be evaluated for each design variable in the considered vicinities causing

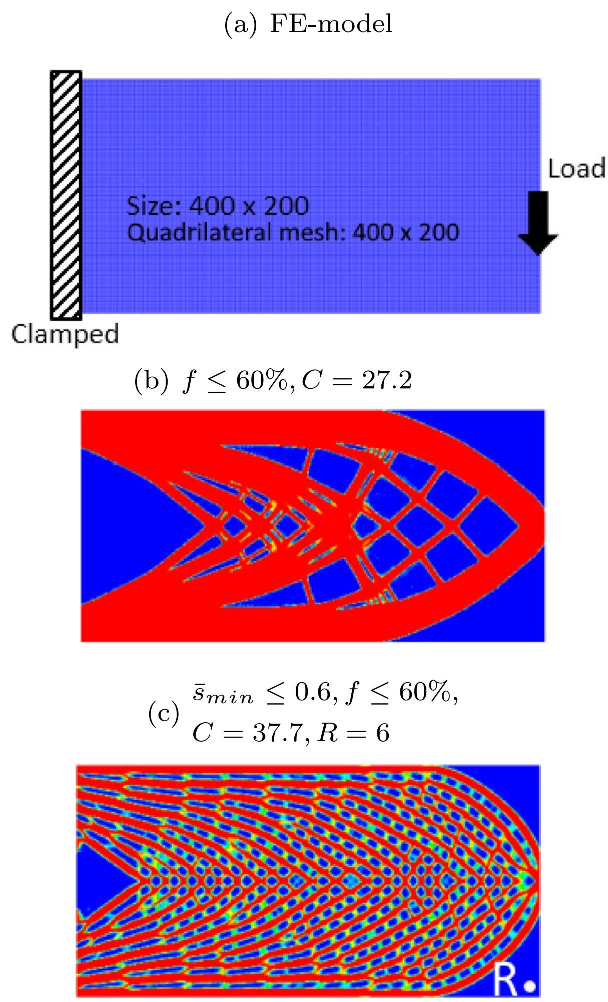

Fig. 9 **a** Rectangular 2D design domain discretized by a 400×200 uniform grid. **b** Classic stiffness topology optimization using a material volume fraction $f = 60\%$. **c** As the classic topology optimization in (**b**) but including the proposed constraint defined in Eq. (15). The lowest singular value $\bar{s}_{min}$ is constraint to be less or equal to 0.6 using a radius $R = 6$ equivalent to 6 finite elements, see the white circle in the figure for reference

matrix-vector-multiplications. The number of these operations is directly dependent on the radius R as the number of design variables in the considered vicinities is proportional to R^3. That means that from numerical costs point of view, the suggested approach is efficient for rather smaller radii R. For the considered examples in the following section $R < 10R_f$ is applied.

5 Examples

5.1 A 2D cantilever beam

A simple 2D example is applied in the following for demonstrating the characteristics of the proposed approach compared to the classical topology optimization. Figure 9a shows a rectangular 2D design domain discretized by a 400×200 uniform grid using fully integrated four-node plain stress elements in SIMULIA Abaqus (CP4S) having the dimensions 1×1. An elastic material is applied having a Poisson ratio of 0.3. The left edge of the design domain is fully clamped and an external force is applied to the midpoint at the right edge. Figure 9b shows the result of the classic topology optimization using a material volume fraction of $f = 60\%$.

Figure 9c shows the result additionally applying the proposed constraint defined in Eq. (15) constraining the lowest singular value $\bar{s}_{min} \leq 0.6$ using a radius $R = 6$ equivalent to 6 finite elements. The optimization iteration history is shown in Fig. 10 for the optimization result shown in Fig. 9c. It can be observed that the number of optimization iterations is 73 when applying the additional constraint for the lowest singular value. The number of optimization iterations of the design in Fig. 9b is 55. Hence, the optimization convergence iterations are barely impacted by the additional constraint for the lowest singular value $\bar{s}_{min}$ which is also observed for the other numerical experiments.

Figure 12 shows the optimization results when constraining the lowest singular value $\bar{s}_{min}$ to be 0.60, 0.50 and 0.40 for a radius of the included design variables for the decomposition (SVD) being $R = 6$ and $R = 12$, respectively. Note, that the optimizations in Fig. 12 have no volume constraint applied. One sees that the obtained maximal member sizes are given by $l_{max} = \bar{s}^*_{min} 2R$ as explained in Sect. 4.4. However, small members appear and the radius of the sensitivity filter gives the minimum member size $l_{min} = 2R_f$.

Using the present geometric dimensionality control we yield lattice-like designs for 2D, see Fig. 12, being reasonable similar to the results obtained using local volume constraint approaches for 2D design domains in Wu et al. (2017, 2018) and Schmidt et al. (2019). However, the present approach seems to have an advantage over the local volume constraint approaches. The lattice members obtained

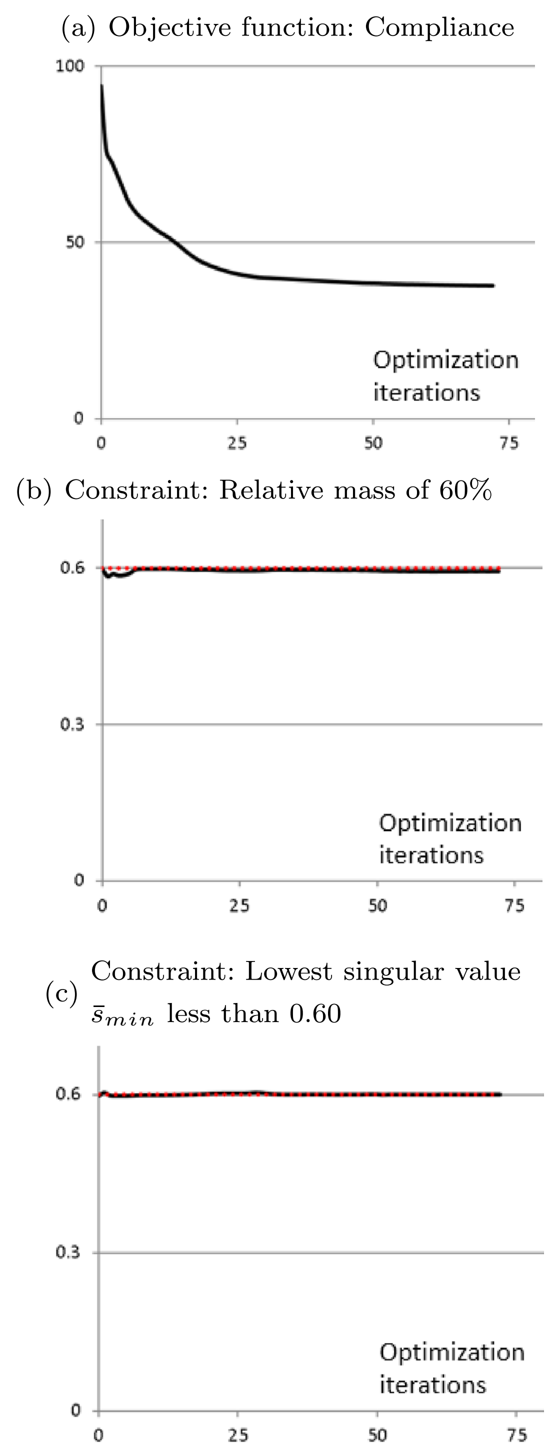

Fig. 10 Optimization iteration convergence history for **a** minimizing the compliance subject to a **b** relative mass constraint of 60% and to the **c** present approach constraining the lowest singular value $\bar{s}_{min}$ to be less than 0.60 for a Radius $R = 6$

using the local volume constraints typically suffer from reducing sizes when approaching intersections and junctions assembling the lattices. However, the results obtained using the present approach seem not to have that drawback.

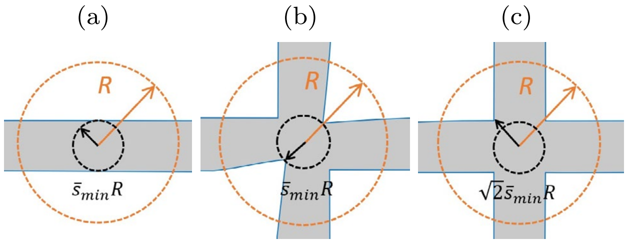

Fig. 11 Smallest singular value for **a** a straight 2D lattice bar and for two lattice joints where **b** fulfills the geometric dimensionality constraint using an unsymmetrical joint and **c** violates the same by $\sqrt{2}$.

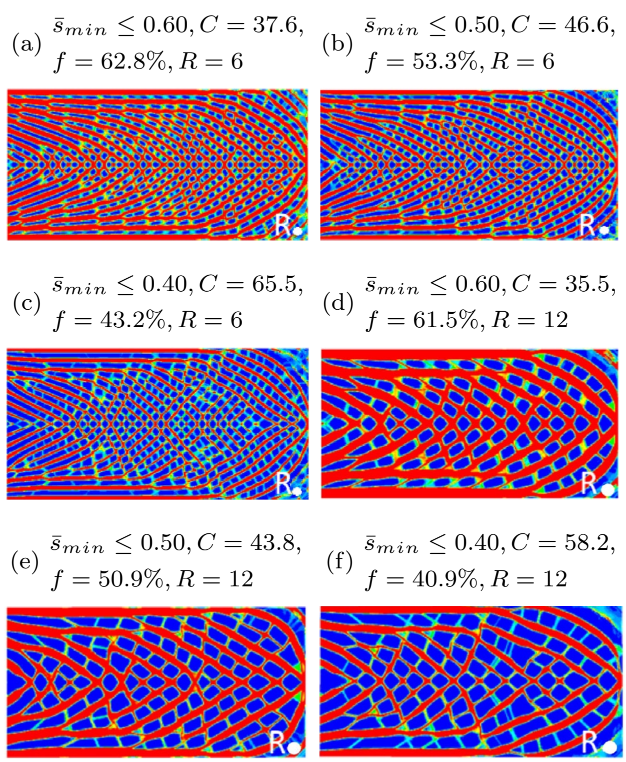

Fig. 12 The lowest singular value is constraint **a**–**c** by $\bar{s}^*_{min}$ which decreases from 0.6 to 0.4 using a radius of $R = 6$ equivalent to 6 finite elements, see the white circle in the figures for reference. Thereby, the member sizes are decreased yielding an increase in compliance C as well as lower relative material volume f. The structures **d**–**f** are optimized using the same set up but applying a larger radius. Comparison of optimized **a**–**c** to **d**–**e** structures shows that increasing the radius R causes larger member sizes having larger distances between them which results in higher stiffness but also less mass. Note, that no symmetry is enforced but the solutions are still prominently symmetrical

The numerical experiments show that the obtained results are less responsive to the choice of the penalty p in Eq. 14 than the local volume constraint, see for example Schmidt et al. (2019). Figure 11 shows the smallest singular value for a 2D model. Figure 11a shows it for a straight lattice and Fig. 11b, c show two joints for a lattice

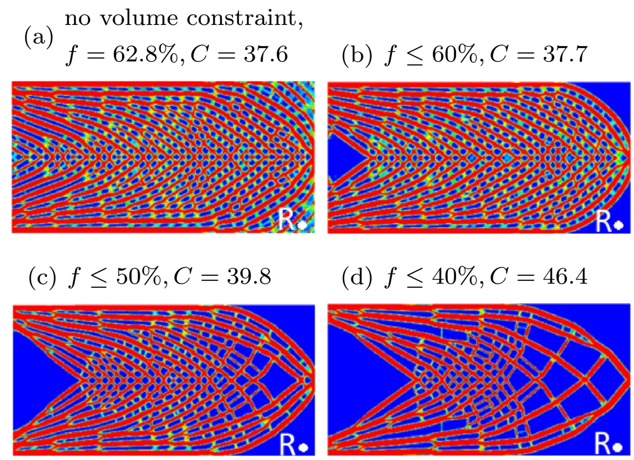

Fig. 13 All designs are optimized constraining the lowest singular value $\bar{s}_{min}$ to be less or equal to 0.6 using a radius $R = 6$, see the white circle in the figures for reference. In **a** no volume constraint is applied whereas in **b**–**d** a volume constraint decreasing from 60 to 40% is considered

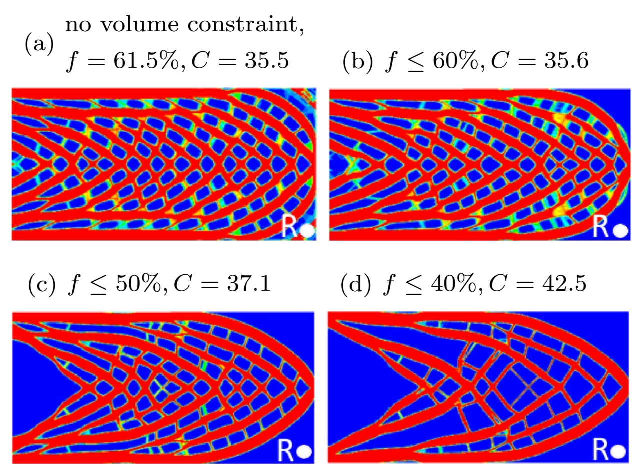

Fig. 14 All designs are optimized constraining the lowest singular value $\bar{s}_{min}$ to be less or equal to 0.6 using a radius $R = 12$, see the white circle in the figures. In **a** no volume constraint is applied whereas in **b**–**d** a volume constraint decreasing from 60 to 40% is considered

structure. Figure b shows that the geometric dimensionality is only enforced in one direction and the optimization algorithm can generate an unsymmetrical joint fulfilling the constraint. Secondly, Fig. 11c shows a joint violating a constraint value for $\bar{s}_{min}R$. One sees that the relative violating value is always $\sqrt{2}\bar{s}_{min} \leq \bar{s}^\star_{min}$ or $\bar{s}_{min} \leq \bar{s}^\star_{min}/\sqrt{2}$ independently upon the constraint value $\bar{s}^\star_{min}$ and the R parameter and thereby, the relative violating magnitude is independent upon the choice of the penalty p in Eq. 14. These two theoretical observations support the

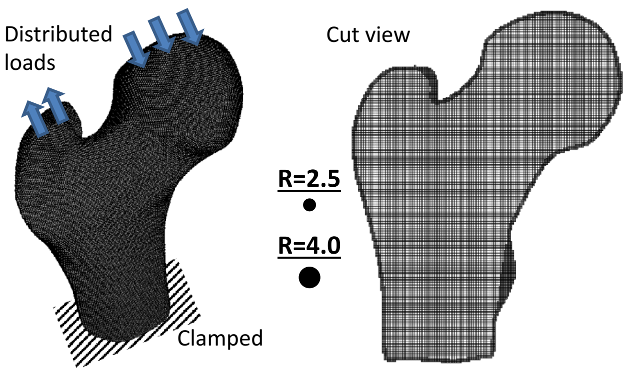

Fig. 15 Discretized femur model consisting of 1,090,793 hexahedral elements. The model is fully clamped at the bottom and two sets of distributed forces are applied at the top. The elements at the outer surface are not part of the design domain. Radii of 2.5 and 4.0 are applied for evaluating the geometric dimensionality control constraints

numerical observations in comparison to the local volume constraints.

Figures 13 and 14 show the effect of adding a global volume constraint to the optimization formulation. Generally, one sees that the classic volume constraint for topology optimization works well when also constraining the lowest singular value. The material volumes of the designs shown in Figs. 13a and 14a optimized without material volume constraints are just slightly higher than the constraining value of the lowest singular value $\bar{s}_{min}$. However, these designs have some intermediate densities for the low strain energy density areas of the design domain. Figures 13b and 14b show that by adding a volume constraint similar to the constraint value of the lowest singular value then these intermediate densities are removed.

Figures 13 and 14 show the results applying the constraint proposed in Eq. (15). We yield designs having satisfying solid\void representations in a fairly low number of optimization iterations and most important, objective function values of the compliance being almost similar to the objective values optimized without the volume constraints. Therefore, the present results as well as additional numerical experiments indicate that for obtaining solid\void 2D optimization solutions then one should apply a volume constraint being the same or lower than the constraint for the lowest singular value.

5.2 Bone infill design

The present section addresses the possibility of generating a lattice infill structure and membrane infill structures for

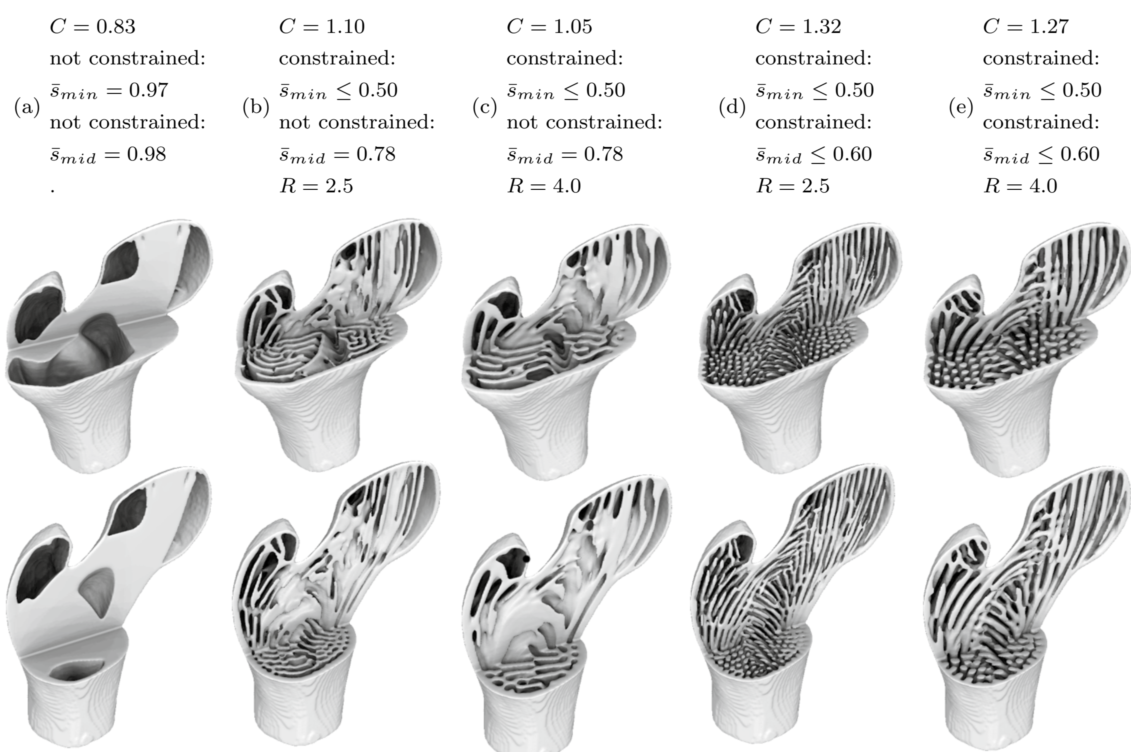

Fig. 16 Topology optimized infills for a femur using a relative material mass fraction of 0.50. The outer surface is not part of the design domain. **a** Classic stiffness optimization subject to a mass constraint. Topology optimization obtaining membrane infills (**b**, **c**) and lattice infills (**d**, **e**) by constraining the singular values

a femur, respectively. The femur finite element model, see Fig. 15, consists of 1,090,793 hexahedral elements (C3D8) each having the size $1 \times 1 \times 1$ yielding 3,420,603 DOFs. The corresponding system of equations is solved using an iterative algebraic multi-grid solver, Dassault Systèmes (2021a). An elastic material is applied having a Poisson ratio of 0.3. The 3D femur model is fully clamped at the bottom and two sets of distributed forces are applied at the top. The elements at the outer surface are not part of the design domain. Figure 16a shows the standard topology optimization result maximizing the stiffness subject to a relative volume constraint of 0.50 but no additional constraints. The same relative volume constraint value is applied for the following numerical experiments, see Fig. 16b–e, but additional constraints are added for the $\bar{s}_{min}$ and $\bar{s}_{mid}$, respectively. The constraining singular values $\bar{s}_{min}$ and $\bar{s}_{mid}$ are estimated to be around 0.58 using the lattice approximation for $f = 0.50$ outlined in Sect. 4.4.

Only the first singular value $\bar{s}_{min}$ is constrained to be 0.50 for the optimization results shown for $R = 2.5$ in Fig. 16b and for $R = 4.0$ in Fig. 16c, respectively. These results consist mainly of membrane components having the thickness $2R\bar{s}_{min}$ as infill for the femur which is expected as membrane components are stiffer than lattice structures, see Sigmund et al. (2016). In addition, the obtained components are rather similar to the prior results presented in Schmidt et al. (2019), Wu et al. (2017, 2018) using local volume constraint also yielding membrane-like structures for the infill of the femur. Thus, the present membrane designs obtained using a single constraint for the first singular value $\bar{s}_{min}$ and the previous reported designs in Schmidt et al. (2019), Wu et al. (2017, 2018) using a local volume constraint would not be feasible for having blood diffusing through the structure transporting the nutrition as well as being infeasible for many Additive Manufacturing processes based upon powder as the powder would be trapped inside the design after printing.

Subsequently, we constraint both the first singular value $\bar{s}_{min}$ to be 0.50 and the second singular value $\bar{s}_{mid}$ to be 0.60 for enforcing a design having lattice infill components as shown in Fig. 16d and e, respectively. The optimized structures now have distinct lattice components as infill compared to the membrane infill results in Fig. 16b and c. However, the membrane infill structures have around 20% higher stiffness than the lattice infill structures for both a radius of $R = 2.5$ and $R = 4.0$, respectively.

Consequently, the present geometric dimensionality control allows us to both obtain membrane designs similar to solutions obtained using local volume constraint but also most important to obtain designs being true lattice designs having open cell structures. Thereby, open lattice cell structures feasible for Additive Manufacturing (getting the powder out after manufacturing) as well as allowing another media to flow through the optimized structures are achieved.

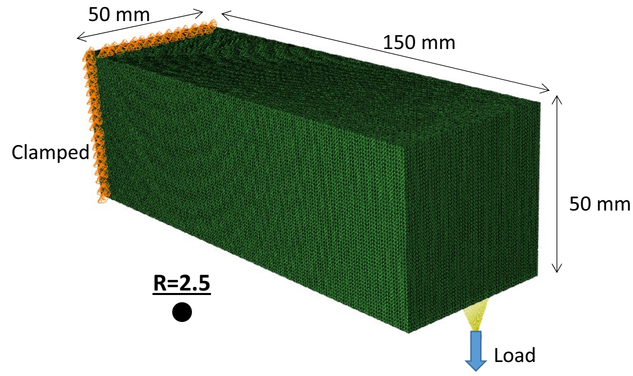

Fig. 17 Discretized beam model consisting of 2,172,846 second order tetrahedral elements. The model is fully clamped on the left side and loaded at a reference node of a distributed coupling on the right side. The radius of $R = 2.5$ is set for the applied geometric dimensionality control constraints

5.3 Strength optimization of a 3D cantilever beam

The present section addresses strength optimization of a 3D cantilever beam by minimizing the mass subject to a stress constraint of $s_C = 70$ N/mm^2 as defined in Eq. (2). An elastic material is applied with a Young modulus of 210, 000 N/mm^2 and a Poisson ratio of 0.3, respectively. Figure 17 shows the dimensions of the cantilever beam being fully clamped at one end of the beam and applied to a load of 800 N at the reference node of the distributed coupling. All stresses of the elements being attached to the distributed coupling are excluded for the stress constraint in Eq. (2) for avoiding stress singularities. The 3D cantilever beam mesh consists of 2,172,846 higher order tetrahedron elements (C3D10HS) for improved bending results, see Dassault Systèmes (2021a), yielding 9,282,066 DOFs. The corresponding system of equations is solved using the iterative algebraic multi-grid solver, Dassault Systèmes (2021a). The present element uses a unique 11-point integration scheme, providing a superior stress visualization with coarse meshes as it avoids errors due to the extrapolation of stress components from the integration points to the nodes.

Figure 18 shows the optimized results having constraints imposing geometric control except from the design in

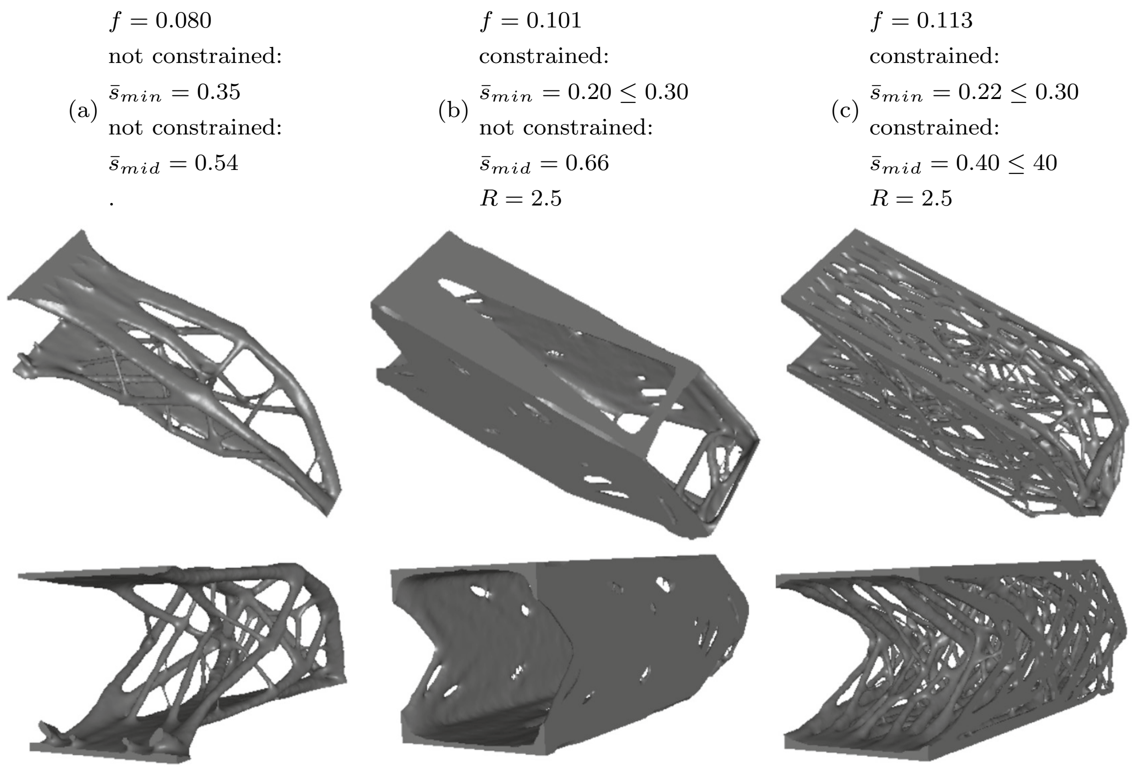

Fig. 18 Strength optimization results for the beam in Fig. 17 where the mass is minimized subject to a stress constraint. **a** Design obtained without geometric dimensionality constraint. **b** Design using geometric control constraining s_{min} so no structural members can have a thickness larger than 1.5. **c** Design obtained applying an additional constraint for s_{mid} consisting entirely of lattice members with a maximum cross section thickness of 1.5 and width of 2.0, respectively

Fig. 18a which has no geometric dimensionality constraints. The designs in Fig. 18b, c have a geometric constraint for $\bar{s}_{min}$ to be less than 0.3 for a radius of $R = 2.5$ so no structural members of the optimized designs can have a thickness larger than 1.5. We want to enforce a design dominated by membrane members for the design in Fig. 18b. Furthermore, we want to enforce a design consisting of lattice members for the design in Fig. 18c. The constraining values for $\bar{s}_{min}$ and $\bar{s}_{mid}$ are estimated to be around 0.28 using the lattice approximation outlined in Sect. 4.4. Hence, we apply a radius of $R = 2.5$ for both $\bar{s}_{min}$ and $\bar{s}_{mid}$ constraints which have to be less than 0.3 and 0.4, respectively.

The design having no geometric constraints shown in Fig. 18a has a mass of 8%. Whereas the design in Fig. 18b constrained by the lowest singular value $\bar{s}_{min}$ has a mass of 10.1%. The present design is mainly a full membrane solution except close to the loading point where a few lattice members are present. Therefore, the optimization in Fig. 18c constrained by the lowest singular value $\bar{s}_{min}$ and the second singular value $\bar{s}_{mid}$ has a mass of 11.3%. Thereby, we have a numerical evidence that membrane structures are not just ideal for stiffness designs but also for strength designs. The lattice design in Fig. 18c is suboptimally for strength designing as the mass is increased by 40% compared to the design in Fig. 18a.

Figure 19 shows the optimization convergence history for the three designs in Fig. 18. It is interesting to observe when only constraining the lowest singular value $\bar{s}_{min} \leq 0.3$ then the constraint is not active by the end of optimization, see Fig. 19c. That means that membrane structure is suboptimal. The constraint just pushes the design in the corresponding direction at the beginning of optimization. Note, the number of optimization iterations is reduced using geometric dimensionality constraints. We also recognize in Fig. 19b that the highest objective function value is obtained applying both dimensionality constraints on $\bar{s}_{min}$ and on $\bar{s}_{mid}$ which is expected as the design space is most restricted. In Fig. 19d the value of $\bar{s}_{mid}$ is tracked also for the cases where it was

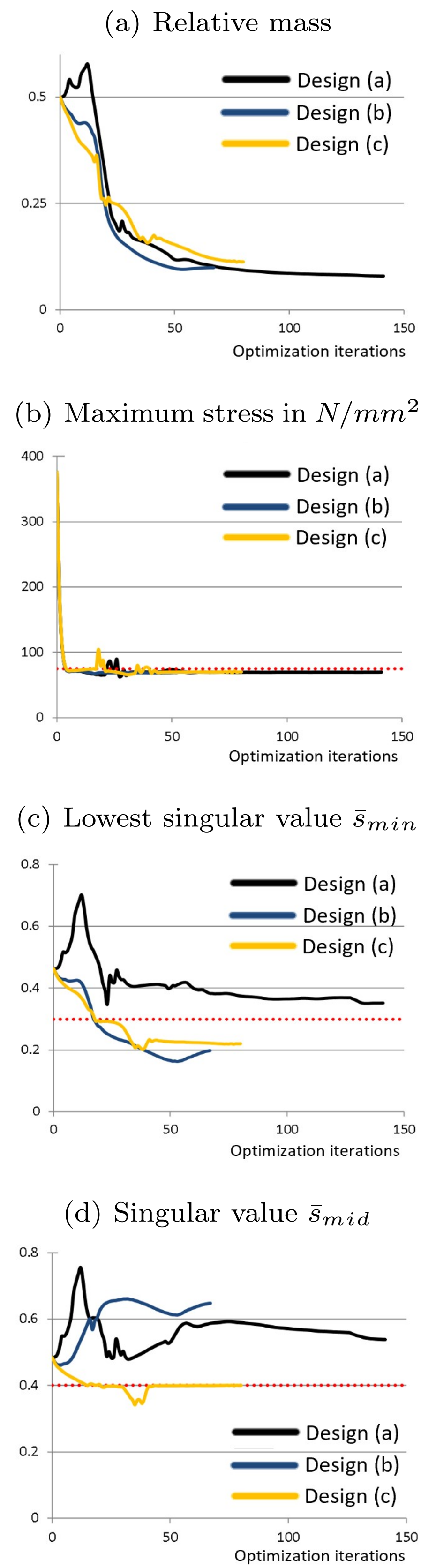

Fig. 19 Optimization convergence history for the three designs in Fig. 18 where the relative mass is minimized subject to a stress constraint $A(s_v) \leq s_C = 70$ N/mm^2. The designs in Fig. 18b, c where obtained applying a constraint $\bar{s}_{min} \leq 0.3$ and for the design in Fig. 18c an additional constraint $\bar{s}_{mid} \leq 0.4$ was applied. The content of this figure is: (a) relative mass, (b) maximum stress, (c) lowest singular value and (d) midle singular value

not constrained being considerably higher than the value for the constrained case.

6 Conclusion

We present a new method for geometric dimensionality control in topology optimization based upon constraining the singular values of the decomposition (SVD) of the design variables in a given radius. The present approach has the following advantages:

- Numerical examples demonstrate that it is possible to obtain solid void optimization results applying a volume constraint being the same or lower than the constraint for the lowest singular value.
- The optimization performance concerning the number of optimization iterations for the present geometric dimensionality control is hardly influenced by the present approach constraining the singular values for the decomposition (SVD) of the design variables.
- Using the present geometric dimensionality control the designs for 2D are similar to the results obtained using local volume constraint approaches. The advantages of the present approach for geometric dimensionality control is that we for 3D can enforce either lattice-like structures or membrane dominated structures. Previous approaches do not allow for these associated considerations in the optimization formulation.
- As expected the numerical experiments show that the membrane structures have the best structural performance for both stiffness and strength compared to the lattice designs. In addition, the numerical experiments show that there is often a very low deficit in the structural performance when enforcing membrane structures comparing to the designs optimized having no constraints for the geometric dimensionality control.

– Lattice designs for 3D structures might not be optimal for stiffness and strength. However, the open lattice cell structures might be desirable for Additive Manufactured (AM) designs with respect to removing the powder after manufacturing as well as allowing another media to flow through the optimized structures, for example, for cooling.
– Previous approaches did not allow for enforcing lattices in continuum topology optimization and at the same control their dimensionality by the radii for the singular values of the decomposition (SVD) of the design variables and as well as the constrain values.

For the present contribution, we focus on the generation of lattice-like structures but also recognized the possibility obtaining membrane dominated structures. In the future work we will also consider the generation of pure membrane-like or shell structures using the constraint proposed in Eq. (17) as this is a permanently asked feature in context of industrial applications.

Funding Open Access funding enabled and organized by Projekt DEAL.

Declarations

Conflict of interest On behalf of all authors, the corresponding author states that there is no conflict of interest.

Replication of results All results presented in this work apply the following parameters for optimization: SIMP using a penalty of 3 a density filter of radius 1.3 relative to 2D or 3D meshes consisting of squares, cubes or tetrahedral elements. The approach presented in Sects. 3 and 4 is implemented using SIMULIA Abaqus Dassault Systèmes (2021a) and SIMULIA Tosca Structure Dassault Systèmes (2021b). Thereby, the present implementation is commercially available to others for both academic and professional applications.

References

Bendsøe MP, Sigmund O (2004) Topology optimization—theory, methods, and applications. Springer-Verlag, Berlin

Bruggi M (2008) On an alternative approach to stress constraints relaxation in topology optimization. Struct Multidisc Optim 36(2):125–141. https://doi.org/10.1007/s00158-007-0203-6

Carstensen JV, Guest JK (2018) Projection-based two-phase minimum and maximum length scale control in topology optimization. Struct Multidisc Optim 58:1845–1860

Dassault Systèmes: SIMULIA Abaqus Documentation, version 2022x edn. (2021a)

Dassault Systèmes: SIMULIA Tosca Structure Documentation, version 2022x edn. (2021b)

Dienemann R, Schumacher A, Fiebig S (2017) Topology optimization for finding shell structures manufactured by deep drawing. Struct Multidisc Optim 56:473–485

Gersborg AR, Andreasen CS (2011) An explicit parameterization for casting constraints in gradient driven topology optimization. Struct Multidisc Optim 44:875–881

Hoffarth M, Gerzen N, Pedersen C (2017) ALM overhang constraint in topology optimization for industrial applications. InProceedings of the 12th world congress on structural and multidisciplinary optimisation, Braunschweig, Germany

Holmberg E, Torstenfelt B, Klarbring A (2013) Stress constrained topology optimization. Struct Multidisc Optim 48(1):33–47. https://doi.org/10.1007/s00158-012-0880-7

Kennedy GJ, Hicken JE (2015) Improved constraint-aggregation methods. Comput Methods Appl Mech Eng 289:332–354. https://doi.org/10.1016/j.cma.2015.02.017

Langelaar M (2017) An additive manufacturing filter for topology optimization of print-ready designs. Struct Multidisc Optim 55:871–883

Langelaar M (2019) Topology optimization for multi-axis machining. Comput Methods Appl Mech Eng 351:226–252

Lazarov BS, Wang F (2017) Maximum length scale in density based topology optimization. Comput Methods Appl Mech Eng 318:826–844

Lazarov BS, Wang F, Sigmund O (2016) Length scale and manufacturability in density-based topology optimization. Arch Appl Mech 86:189–218

Leiva J, Watson B, Kosaka I (2004) An analyticall Bi-Directional growth parameterization to obtain optimal castable topology designs. In10th AIAA/ISSMO Multidisciplinary Analysis and Optimization Conf., Albany, NY, USA

Liu Y, Zhou M, Wei C, Lin Z (2021) Topology optimization of self-supporting infill structures. Struct Multidisc Optim. https://doi.org/10.1007/s00158-020-02805-y

Luo Y, Li Q, Liu S (2019) Topology optimization of shell-infill structures using an erosion-based interface identification method. Comput Methods Appl Mech Eng 355:94–112. https://doi.org/10.1016/j.cma.2019.05.017

Norato JA (2018) Topology optimization with supershapes. Struct Multidisc Optim 58:415–434

París J, Navarrina F, Colominas I, Casteleiro M (2008) Topology optimization of continuum structures with local and global stress constraints. Struct Multidisc Optim 39(4):419–437. https://doi.org/10.1007/s00158-008-0336-2

Schmidt M, Pedersen CBW, Gout C (2019) On structural topology optimization using graded porosity control. Struct Multidisc Optim 60:1437–1453

Seyranian A (1987) Multiple eigenvalues in optimization problems. J Appl Math Mech 51(2):272–275

Seyranian AP, Lund E, Olhoff N (1994) Multiple eigenvalues in structural optimization problems. Struct Optim 8:207–227

Sigmund O, Petersen J (1998) Numerical instabilities in topology optimization: a survey on procedures dealing with checkerboards, mesh-dependencies and local minima. Struct Optim 16:68–75

Sigmund O, Maute K (2013) Topology optimization approaches: a comparative review. Struct Multidisc Optim 48(6):1031–1055. https://doi.org/10.1007/s00158-013-0978-6

Sigmund O, Aage N, Andreassen E (2016) On the (non-)optimality of Michell structures. Struct Multidisc Optim 54(2):361–373. https://doi.org/10.1007/s00158-016-1420-7

Strömberg N (2010) Topology optimization of structures with manufacturing and unilateral contact constraints by minimizing an adjustable compliance-volume product. Struct Multidisc Optim 42:341–350

Vatanabe SL, Lippi TN, de Lima CR, Paulino GH, Silva EC (2016) Topology optimization with manufacturing constraints: a unified projection-based approach. Adv Eng Softw 100:97–112

Verbart A, Langelaar M, van Keulen F (2015) Damage approach: a new method for topology optimization with local stress constraints. Struct Multidisc Optim 53(5):1081–1098. https://doi.org/10.1007/s00158-015-1318-9

Wu J, Clausen A, Sigmund O (2017) Minimum compliance topology optimization of shell-infill composites for additive manufacturing. Comput Methods Appl Mech Eng 326:358–375

Wu J, Aage N, Westermann R, Sigmund O (2018) Infill optimization for additive manufacturing-approaching bone-like porous structures. IEEE Trans Vis Comput Graph 24(2):1127–1140

Zhang S, Norato JA, Gain AL (2016) A geometry projection method for the topology optimization of plate structures. Struct Multidisc Optim 54:1173–1190

Zhang S, Gain AL, Norato JA (2018) A geometry projection method for the topology optimization of curved plate structures with placement bounds. Int J Numer Methods Eng 114(2):128–146

Zhou M, Lazarov BS, Wang F, Sigmund O (2015) Minimum length scale in topology optimization by geometric constraints. Comput Methods Appl Mech Eng 293:266–282